



HAL
open science

Grain Boundary Sliding and Strain Rate Sensitivity of Coarse and Fine/Ultrafine Grained 5083 Aluminum Alloys

A. Goyal, V. Doquet, Amade Pouya

► **To cite this version:**

A. Goyal, V. Doquet, Amade Pouya. Grain Boundary Sliding and Strain Rate Sensitivity of Coarse and Fine/Ultrafine Grained 5083 Aluminum Alloys. Metallurgical and Materials Transactions A, 2019, 51 (3), pp.1109-1122. 10.1007/s11661-019-05583-5 . hal-02481466

HAL Id: hal-02481466

<https://hal.science/hal-02481466v1>

Submitted on 9 Nov 2020

HAL is a multi-disciplinary open access archive for the deposit and dissemination of scientific research documents, whether they are published or not. The documents may come from teaching and research institutions in France or abroad, or from public or private research centers.

L'archive ouverte pluridisciplinaire **HAL**, est destinée au dépôt et à la diffusion de documents scientifiques de niveau recherche, publiés ou non, émanant des établissements d'enseignement et de recherche français ou étrangers, des laboratoires publics ou privés.

Grain Boundary Sliding and Strain Rate Sensitivity of Coarse and Fine/Ultrafine Grained 5083 Aluminum Alloys



A. GOYAL, V. DOQUET, and A. POUYA

The viscoplastic behavior of coarse and bimodal fine/ultrafine grained (F/UFG) Al5083 alloy was investigated between 20 °C and 200 °C through tensile tests at various strain rates, and stress relaxation tests to deduce the strain rate sensitivity (SRS). The plastic strain fields were measured by correlation of SEM images. In the F/UFG material at high temperature, very high strains were measured in shear bands which sometimes crossed the whole gage width and exhibited intensive grain boundary sliding (GBS). Both the SRS and ductility rose with the temperature, and as the strain rate decreased, mainly due to a rising contribution of GBS, which accommodated a much larger fraction of the global strain in the F/UFG material. The boundary between the temperature–strain rate domains where grain refinement led either to strengthening or to softening was determined. Finite element simulations of tension and relaxation tests with viscoplastic grains and sliding grain boundaries captured the macro-scale behavior of the F/UFG material. It also provided some insight into the mechanisms of correlated and cooperative GBS and grain rotation along percolation paths (both inter and intragranular), probably, responsible for macro shear banding.

<https://doi.org/10.1007/s11661-019-05583-5>

© The Minerals, Metals & Materials Society and ASM International 2019

I. INTRODUCTION

ULTRAFINE grained (UFG) metals or alloys generally exhibit a substantially higher flow stress than their coarse grained (CG) counterparts, at room temperature. Their fracture strain is most often lower than that of CG materials at room temperature. However, it tends to increase as the strain rate decreases due to of a modification in the plastic strain distribution leading to a lot of diffuse—and thus harmless—micro-bands, instead of a few sharp and intense shear bands observed at higher rates.^[1–3]

Regarding the high-temperature behavior of these materials, most investigations focused on the superplastic regime, characterized by a strain rate sensitivity (SRS) close to 0.5, which is controlled by grain boundary sliding (GBS)^[4,5] and is observed at comparatively lower temperatures than in CG materials.^[6–9] The intermediate range between room temperature and

superplastic regime has, comparatively, received much less attention.

However, it has been shown by Kapoor *et al.*^[10] that above a strain rate-dependent temperature, instead of GBS-induced hardening, GBS-induced softening occurs in Al-1.5Mg. Since many potential applications of UFG alloys involve heating above ambient temperature, it is necessary to determine the temperature and strain rate domains in which a beneficial effect of the ultrafine microstructure can be expected. This is one of the purposes of this study on Al 5083 alloy.

Since the evolutions in ductility with strain rate mentioned above seem to correlate with the degree of strain localization, and thus to the SRS, this parameter was measured as a function of temperature and strain rate, through stress relaxation tests in CG and UFG Al 5083 alloys. The plastic strain fields in these materials were measured by digital image correlation (DIC) before and after tensile tests run at room or high temperature. The discontinuities induced by GBS along the micro-grids laid on the surface for digital image correlation (DIC) were used to estimate the contribution of GBS to the overall deformation, which appeared to explain most of the temperature and strain rate-dependence of the SRS.

In the seventies, Raj and Ashby^[11] proposed an analytical model of grain boundary sliding accommodated either elastically, or by diffusion. They formulated a linear, threshold-free relation between the GB sliding

A. GOYAL and V. DOQUET are with the Laboratoire de Mécanique des Solides, UMR 7659 CNRS, Ecole Polytechnique, 91128, Palaiseau, France. Contact e-mail: doquet@lms.polytechnique.fr A. POUYA is with the Laboratoire Navier (IFSTTAR, CNRS, ENPC), Paris-Est University, 77455 Champs sur Marne, France.

Manuscript submitted August 30, 2019.

	Journal : MMTA	Dispatch : 3-12-2019	Pages : 14
	PIPS No. : 5583	<input type="checkbox"/> LE	<input type="checkbox"/> TYPESET
	MS Code :	<input type="checkbox"/> CP	<input type="checkbox"/> DISK

74 rate and the resolved shear stress, in which viscosity
75 increased with the roughness of the GB, and with the
76 presence of second phase particles along its length.
77 Ashby and Verral^[12] introduced a GBS-induced neigh-
78 boring grains switching mechanism, without any elon-
79 gation or change in crystal orientation. They predicted a
80 grain size-dependent evolution of the SRS associated
81 with the transition from this deformation mechanism to
82 dislocation-controlled creep, as the strain rate rises.

83 A 2D, plane strain finite element analysis of creep
84 with free grain boundary sliding accommodated by
85 elasticity and diffusion processes was later developed by
86 Crossman and Ashby,^[13] who considered a regular array
87 of hexagonal grains with power law creep inside. They
88 investigated the influence of the viscous stress exponent,
89 n , inside the grains, and of the strain rate on the
90 contribution of GB sliding to the overall deformation.
91 They obtained a modified power law equation for the
92 steady creep rate that predicts an acceleration when
93 GBS occurs, but no modification of the creep exponent.
94 The 2D computational approach of Tvergaard^[14,15] in
95 the eighties was close to that of Crossman and Ashby,
96 but laid emphasis on the consequences of GB sliding in
97 terms of cavities nucleation and growth along the grain
98 boundaries normal to the tensile axis, while Hsia *et al.*^[16]
99 directly introduced a density, of micro-cracks along such
100 GBs and investigated the effect of GB sliding on the
101 growth rate of such cracks. All the works mentioned
102 above considered a periodic array of hexagonal grains.

103 Onck and Van Der Giessen^[17] investigated the effect
104 of microstructural variations on the creep rate of a
105 polycrystalline aggregate with freely sliding boundaries,
106 by slightly perturbing an initially regular array of
107 hexagonal grains. The computed creep rate was
108 enhanced by up to 60 pct by the introduction of some
109 irregularity, due to increased GB sliding.

110 Bower and Winger^[18] proposed a sophisticated 2D
111 crystal plasticity finite element (CPFE) approach where,
112 in addition to GB sliding, GB migration assisted by
113 diffusion was modeled. They used a front tracking
114 scheme and adaptive mesh generation techniques to
115 follow the changes in grain structure. The model was
116 used by Agarwal *et al.*^[19] to predict the rate-sensitive
117 SRS of fine-grained (7 to 10 μm) Al5083 alloy above
118 450 °C. Some discrepancies with experimental data were
119 found at low strain rate, but according to Du *et al.*^[20]
120 the introduction of a threshold shear stress for GB
121 sliding improved the predictions. Both studies were
122 based on the same polycrystalline aggregate with 18
123 irregular grains, taken from a micrograph, as well as the
124 crystal orientations. The simulations were not repeated
125 with different numbers of grains and different sets of
126 orientations, so that their statistical representativeness
127 can be questioned. In addition, only $\{111\}$ (110) slip was
128 considered, while non-octahedral slip systems were
129 found to operate above 200 °C in Al 5083 alloy.^[21]

130 Many authors used molecular dynamics (MD) simu-
131 lations to investigate GB mobility. Qi and Krajewski^[22]
132 used MD to simulate GBS in aluminum at 750 K and
133 reported three regimes depending on the applied stress:
134 (i) at low applied stress, no sliding was observed,
135 indicating the existence of a threshold stress (ii) at

136 intermediate stress, the amount of sliding increased
137 linearly with time, confirming the linear viscous nature
138 of GBS described by Raj and Ashby, and (iii) at high
139 stress, the amount of sliding increased parabolically with
140 time. According to the MD simulations done by Du
141 *et al.*^[23] the segregation of solute atoms (Mg and Si in
142 Al5083 alloy) at GBs affects the threshold stress for GB
143 sliding. While these atomic scale simulations provide
144 valuable insight into the GB deformation mechanisms
145 and their variations from one type of GB to another, it
146 is difficult to get quantitative data, since the simulations
147 are run at pico-seconds time scales and generally include
148 only two neighboring grains, without any triple point, as
149 in a polycrystal.

150 A solution for scale transition was proposed by
151 Warner *et al.*^[24] who performed 2D “atomistics-in-
152 formed” crystal plasticity finite element (CPFE) simu-
153 lations for nano-crystalline copper, with 200 grains and
154 GB constitutive equations derived from prior MD
155 simulations. However, since MD simulations were run
156 for a few specific types of GB (symmetric or asymmetric
157 tilt boundaries), the shear strength of high-angle GBs in
158 CPFE simulations was assigned randomly. A “thermal
159 correction” to the 0 K molecular statics results had to be
160 applied, since the stress levels computed with MD at
161 very high strain rates and 0 K are unrealistically large.

162 Compared to these sophisticated micromechanical
163 approaches, the 2D finite element model including GBS
164 in a phenomenological way developed in the present
165 work is quite simplified. However, it will be shown to
166 capture the mechanical behavior of UFG Al 5083
167 between 20 °C and 200 °C, in a wide range of strain
168 rates, and to provide some insight into the cooperative
169 phenomena (GBS and grain rotation).

170 II. EXPERIMENTAL STUDY

171 A. Experimental Procedures

172 A cast and annealed plate of Al-5083 alloy (with the
173 composition shown in Table I) was used to machine
174 specimens of CG material, or rods for ECAP processing.
175 This as-received material had equiaxed grains with a
176 mean size of 93 μm , and contained coarse dendritic
177 intermetallic particles, mostly along the grain bound-
178 aries, as shown in Figure 1.

179 20 × 20 mm rods cut from the plate were submitted
180 to 3 ECAP passes at room temperature, with a back
181 pressure of 60 MPa, following route C (rotation of the
182 sample by 180 deg between consecutive passes), in a
183 lubricated die, with an angle of 90 deg. The material was
184 then annealed at 200 °C during 6 hours. The resulting
185 microstructure was partly characterized by EBSD, in a
186 Philips Quanta 600 FEG-ESEM, using the hkl software,
187 a tension of 20 KV and a step size of 75 nm. A typical
188 orientation map in a small area along the insertion axis/
189 exit axis plane is presented in Figure 2(b). It proved
190 difficult to reach a good indexation rate with EBSD, but
191 Transmission Kikuchi Diffraction (TKD) on a FIB-cut
192 thin foil allowed a more accurate characterization, and
193 confirmed the grain size statistics issued from EBSD

194 data collected on $100 \times 100 \mu\text{m}$ areas along 3 orthog-
 195 onal planes. The mean grain size was 680 nm, but the
 196 microstructure was heterogeneous, with areas in which
 197 the mean grain size was around 300 nm, as well as less
 198 refined areas, with micron-sized grains (Figure 2(c)).
 199 The fraction of high-angle grain boundaries (*i.e.*, with a
 200 misorientation larger than 15 deg) was around 65 pct.
 201 This fine/ultrafine bimodal microstructure will be

Table I. Chemical Composition of Al 5083 Alloy

Composition	Weight Percent
Mg	5.2
Fe	0.24
Mn	0.45
Si	0.27
Cr	0.09
Al	balance

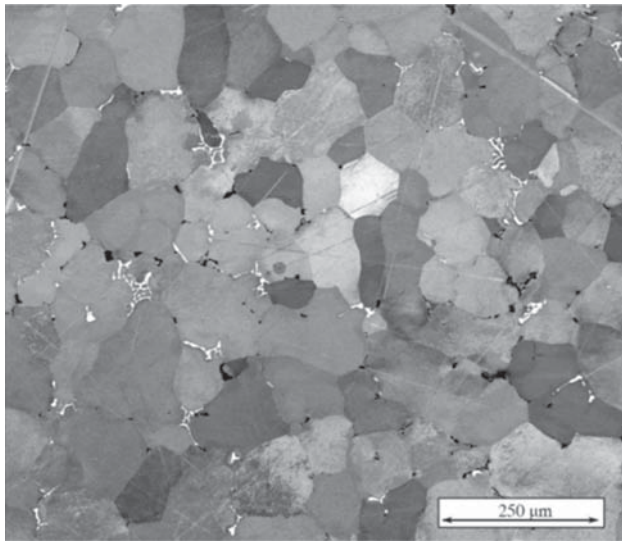


Fig. 1—Microstructure of coarse grained Al5083 Al alloy.

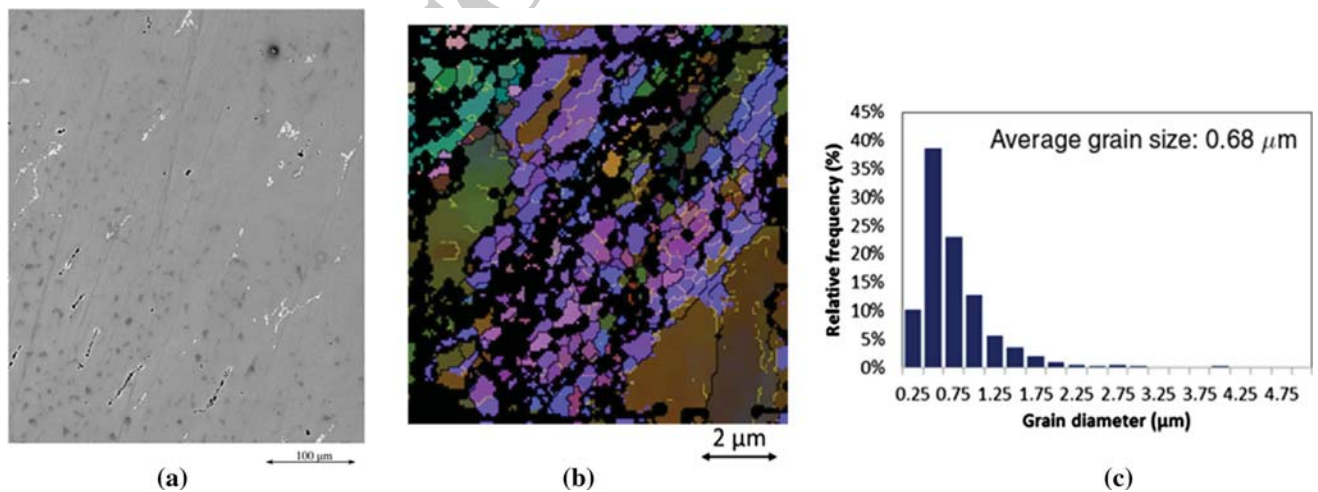


Fig. 2—Microstructure of F/UFG 5083 Al alloy, (a) elongated intermetallic particles, (b) EBSD map (Euler angles), and (c) grain size distribution.

denoted by F/UFG in the following. The grains were
 elongated in the shearing direction of ECAP, at an angle
 around 55 deg. The intermetallic particles were broken
 or debonded and formed rows along the shearing
 direction of ECAP (Figure 2(a)).

Flat dog-bone shaped specimens, with a 17 mm long
 and 4 mm wide gage length, as well as 8 mm high
 cylindrical specimens with a diameter of 8 mm were
 machined parallel to the extrusion axis for tensile tests
 and relaxation tests in compression, respectively. The
 surface of the dog-bone specimens was electro-polished.
 To measure the strain fields using digital image correla-
 tion (DIC), several $600 \times 600 \mu\text{m}$ patches of gold
 grids with a $5 \mu\text{m}$ pitch were printed along the gage
 length, using E-beam lithography. 4096×3775 pixels
 SEM images of the $600 \times 600 \mu\text{m}^2$ areas covered with
 grids were captured before and after the tensile tests.
 The image resolution was thus around $146 \text{ nm pixel}^{-1}$.
 The CmV DIC software^[25] was used with a subset size of
 $4.4 \times 4.4 \mu\text{m}^2$.

The tests at high temperature were run on a servo-hy-
 draulic machine equipped with a thermal chamber. The
 tests were displacement-controlled, and the tensile tests
 were run at different rates, chosen, based on available
 data from the literature, so as capture the transition
 from GB-induced strengthening to GB-induced soften-
 ing, at each temperature. The sample strain was mea-
 sured by monitoring the relative displacement of two
 dots painted near the ends of the gage length. SEM
 images of the micro-grids captured before and after the
 tensile tests were used for DIC.

The relaxation tests were performed in compression
 on cylindrical specimens lubricated with a Teflon spray.
 The samples were first deformed in compression with a
 constant displacement rate corresponding approxi-
 mately to a strain rate of $2 \times 10^{-3} \text{ s}^{-1}$ up to 3 to
 5 pct strain. Then the crosshead displacement was
 stopped for 2 hours, while the stress and strain were
 recorded, each time the load changed by 50 N. Since the
 tests were displacement-controlled, the plastic strain

242 rate, $\dot{\epsilon}_p$ was calculated using the method proposed by
 243 Lee and Hart^[26] as:
 244

$$\dot{\epsilon}_p = - \frac{\dot{\sigma}}{\left[\frac{Kh}{A} - \sigma \right]}, \quad [1]$$

246 where σ is the true stress, K the combined stiffness of the
 247 machine and the sample, and A and h are the cross-section
 248 and height of the specimen, respectively. The strain
 249 rate sensitivity:
 250

$$S = \frac{\partial \ln \sigma}{\partial \ln \dot{\epsilon}} \quad [2]$$

252 was calculated from the slope of plastic strain rate vs
 253 true stress bi-logarithmic plots.

4 B. Macro-scale Behavior

5 Figure 3 compares the tensile curves of CG and F/
 6 UFG alloys at various strain rates, at 20 °C, 100 °C,
 7 and 200 °C. Both materials exhibited serrated flow, due
 8 to dynamic strain aging induced by solute Mg atoms. At
 9 room temperature, grain refinement significantly
 10 increased the flow stress, and reduced the ductility, as
 11 generally reported in the literature for F/UFG alloys. At
 12 100 °C, the difference in flow stress between the two
 13 microstructures was reduced, and at 200 °C, the tensile
 14 curves of the F/UFG alloy lied above or below that of
 15 the CG alloy, depending on the strain rate. For a given
 16 temperature, ductility was strongly strain rate-depend-
 17 ent, as discussed below. Necking was very limited, and
 18 fracture was generally slanted.

19 Figure 4 shows the evolution of the plastic strain rate
 20 with the true stress during the relaxation tests run at
 21 various temperatures on CG and F/UFG materials. The
 22 curves are neither straight nor parallel, which reveals
 23 evolutions of the strain rate sensitivity with the temper-
 24 ature as well as with the strain rate. These evolutions are
 25 represented in Figure 5. For a given temperature and
 26 strain rate, the SRS was higher in the F/UFG material.
 27 In both materials, it rose with the temperature and, at a
 28 given temperature, with decreasing strain rate.

279 Using tension and relaxation data, the temperature
 280 and strain rate domains in which microstructure refine-
 281 ment leads to strengthening (low temperature, high
 282 strain rate regime) or to softening (high temperature,
 283 low strain rate regime) were identified and plotted on
 284 Figure 6. Data from Ko *et al.*^[6] for the same alloy and
 285 from Kapoor *et al.*^[27] for Al-1.5Mg are also plotted, and
 286 are in good agreement with the present results.

287 As mentioned above, in both materials, ductility
 288 above 100 °C increased as the strain rate decreased. The
 289 SRS also rose as the strain rate decreased, and a linear
 290 correlation was found between ductility and SRS, for
 291 each material, as shown in Figure 7. Fracture was thus
 292 controlled by strain localization, that a high SRS tends
 293 to hinder.

294 C. Micro-scale Strain Distribution and Deformation 295 Mechanisms

296 Figure 8 compares strain fields measured in both
 297 materials, at room temperature after a few percent
 298 tensile strain, at $5.8 \times 10^{-5} \text{ s}^{-1}$. In the CG alloy, the
 299 fracture of intermetallic particles located along the grain
 300 boundaries triggered strain localization in short bands
 301 connecting them, without any preferential orientation.

302 By contrast, in the F/UFG alloy, intermetallic parti-
 303 cles, already broken or debonded by ECAP, and aligned
 304 in the same direction as the elongated grains, triggered
 305 the formation of hundreds of micron-long shear bands.
 306 At this temperature ($0.34 T_{\text{melting}}$), grain boundary
 307 sliding in this material produced measurable discontinu-
 308 ities in the grids only in stress concentration areas,
 309 near fractured particles (Figure 9).

310 At 100 °C ($0.43 T_{\text{melting}}$) and above, GB sliding was
 311 observed in the CG material (Figure 10).

312 To estimate the frequency of this phenomenon, the
 313 number of sliding GBs intercepted by a series of parallel
 314 lines was counted, and was divided by the total number
 315 of GBs intercepted by the same lines. To estimate the
 316 strain due to GBS, the micro-grids shifts, u , parallel to
 317 the tensile axis were measured along a series of
 318 transverse grid lines of total length t , and Bell and
 319 Langdon's formula^[28]:

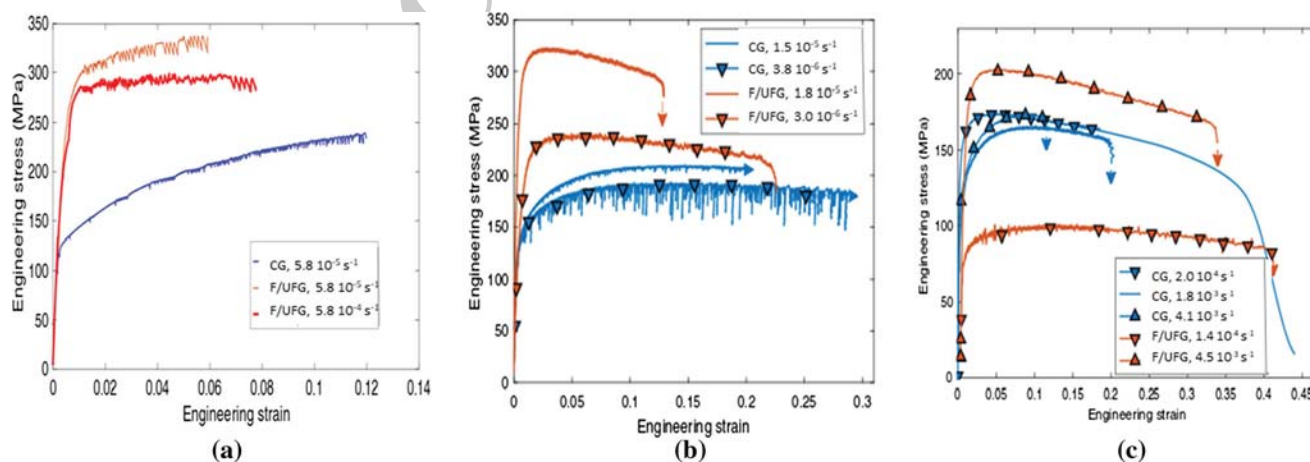


Fig. 3—Tensile curves (a) at room temperature, (b) 100 °C, and (c) 200 °C.

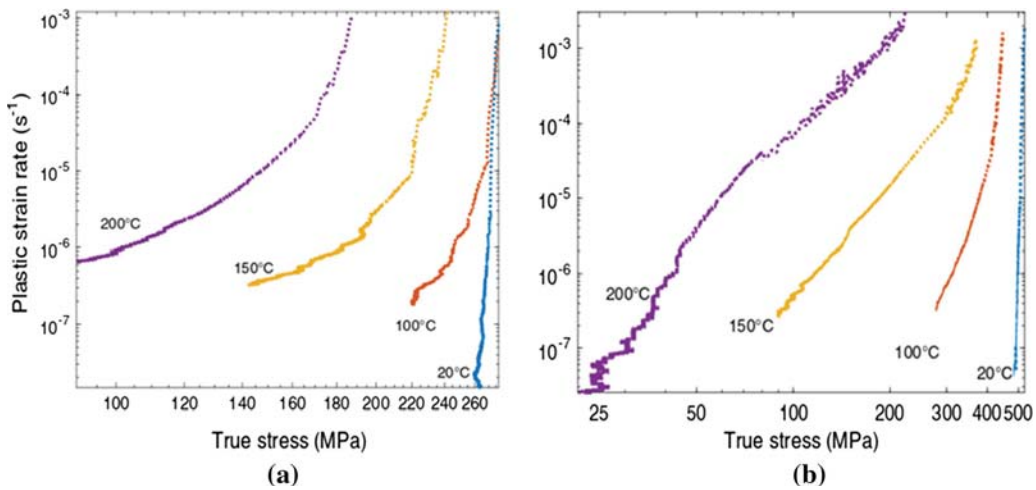


Fig. 4—Stress relaxation curves for (a) CG and (b) F/UFG materials.

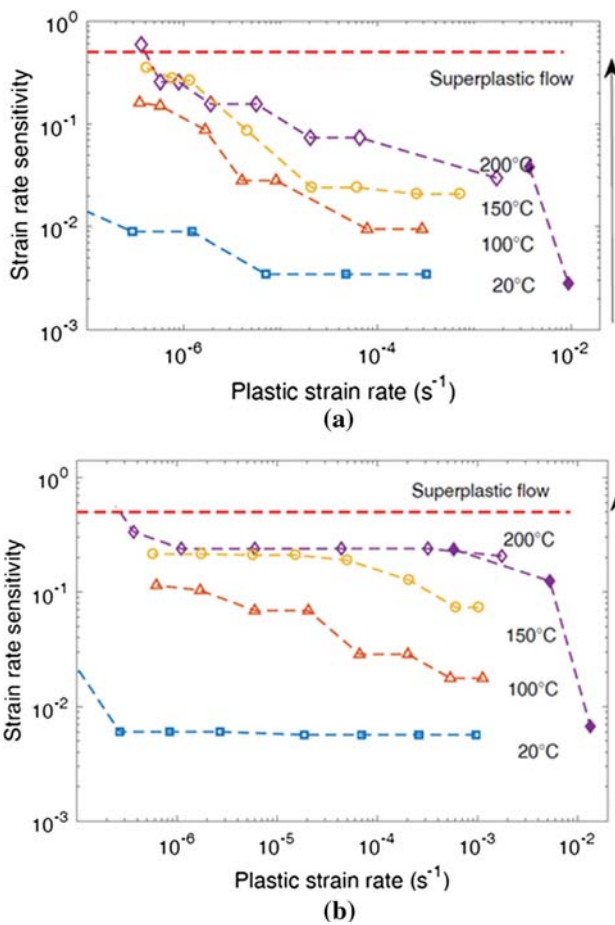


Fig. 5—Evolutions of the strain rate sensitivity for (a) CG and (b) F/UFG materials.

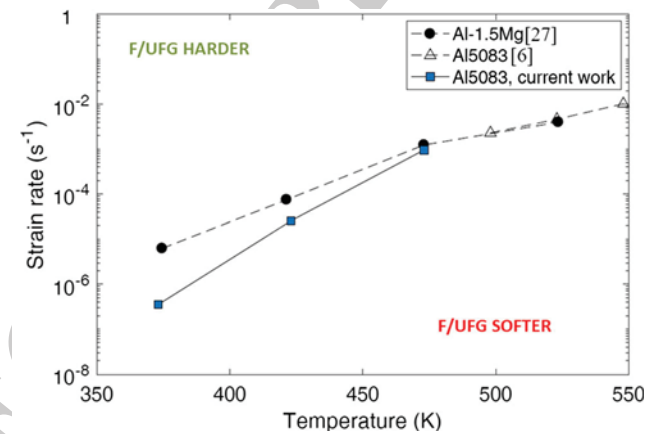


Fig. 6—Domains of grain boundary-induced hardening or softening.

where θ denotes the angle between a grain boundary and the tensile axis—was used. At 100 °C, 9.5 pct of the GBs had sld after 6 pct tensile strain at $1.5 \times 10^{-5} \text{ s}^{-1}$, but this mechanism accounted only for 0.6 pct of the global strain. At 200 °C ($0.55 T_{\text{melting}}$) 44 to 68 pct of the grain boundaries had sld, depending on the strain rate and strain level, but the contribution of this mechanism to the global strain remained limited to 0.8 to 3.8 pct, as reported in Table II.

Figure 11 shows strain maps in F/UFG samples deformed to fracture at 100 °C and 200 °C. Very high strains—up to 50 pct at 100 °C and 90 pct at 200 °C—are measured inside shear bands that sometimes cross the whole gage width.

Strain localization and void sheeting inside such bands led to slanted fracture. A zoom inside such a band reveals intensive grain boundary sliding (Figure 12).

The method described above was used to estimate the contribution of GBS to the global strain. Since the orientation of each sliding GB was difficult to measure

320

$$\epsilon_{\text{GBS}} = \frac{1}{t} \sum_0^t u \times \tan(\theta), \quad [3]$$

in that case, a common value of 55 deg representative of the orientation of GBs after ECAP was assumed for the angle θ in Eq. [3]. The results are reported in Table III. While for the CG alloy, GBS accounted for less than 4 pct of the global strain, in the F/UFG alloy, it accounted for up to 29 pct (and even up to 80 pct within intense shear bands). As expected of a thermally-activated phenomenon, it increased with the temperature, and for a given temperature, as the strain rate decreased.

For the F/UFG alloy, the measured SRS correlates directly with the contribution of GBS, as illustrated by Figure 13.

III. MODELING AND SIMULATION

A 2D, infinitesimal strain, plane stress model with an isotropic viscoplastic behavior for the grains and elastic-viscous sliding interfaces was developed, using the DISROC finite element code.^[29] No attempt to capture the mechanical anisotropy probably induced by the crystallographic texture inherited from ECAP was made. The aim was rather to capture the effects of strain rate and temperature on the uniaxial macroscopic response of the F/UFG material, and to use the

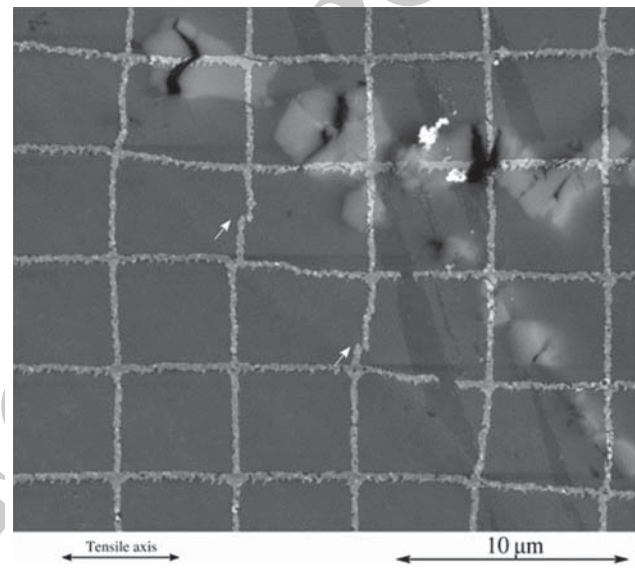
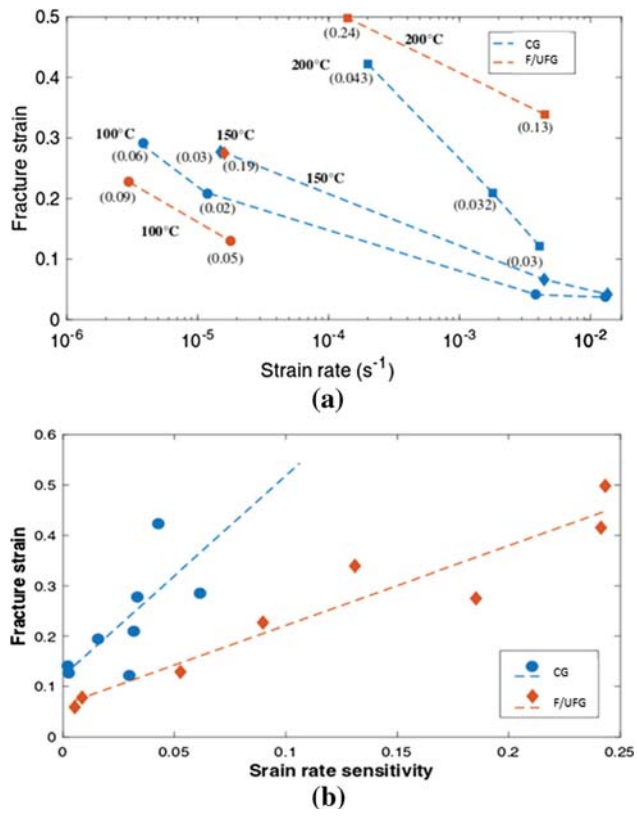


Fig. 7—(a) Effect of the strain rate on ductility, and (b) correlation of ductility with the SRS.

Fig. 9—Grain boundary sliding at room temperature in the F/UFG material triggered locally by the stress concentration near broken intermetallic particles.

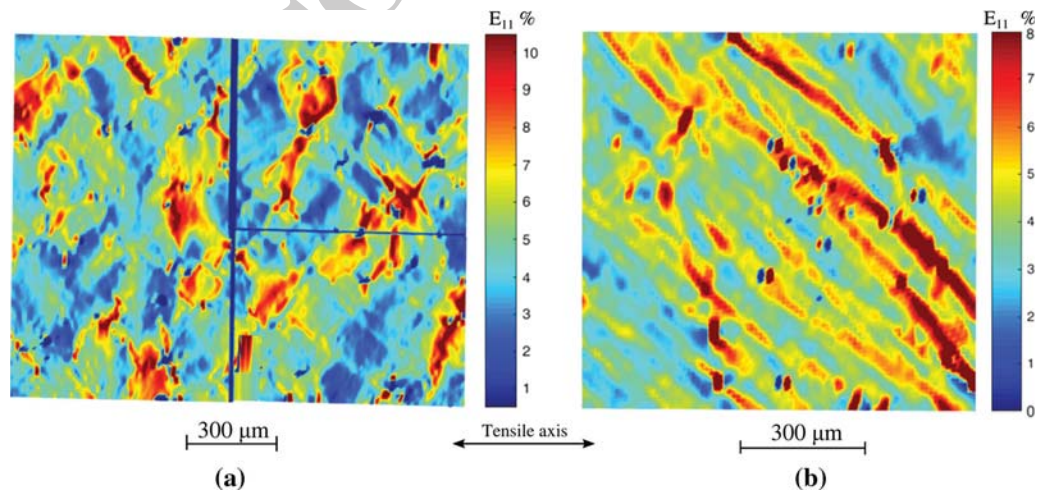


Fig. 8—Strain fields measured at room temperature during tensile tests at $6 \times 10^{-5} \text{ s}^{-1}$ (a) in the CG materials strained by 5.1 pct and (b) in the F/UFG material strained by 4.3 pct.

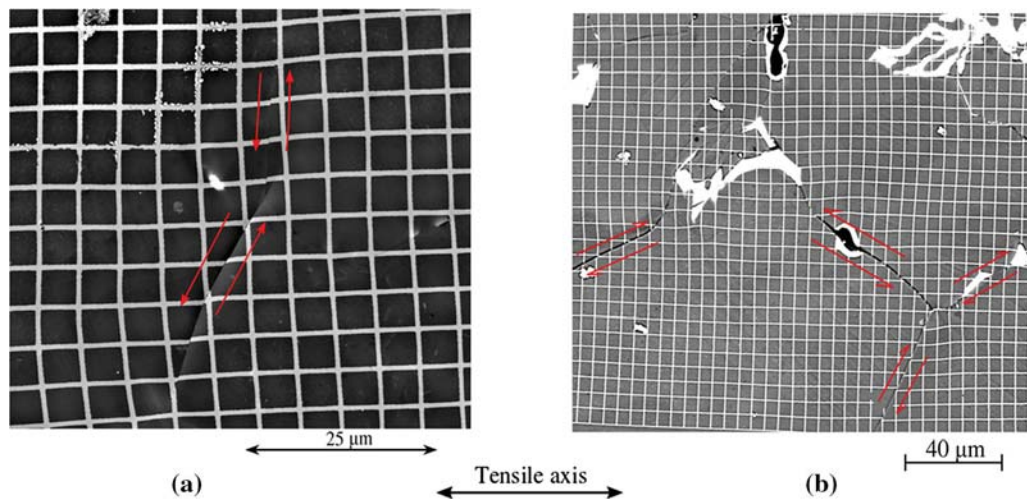


Fig. 10—Grain boundary sliding in CG samples: (a) after 6.5 pct strain at $1.5 \times 10^{-5} \text{ s}^{-1}$ at 100 °C and (b) after 4.7 pct strain at $7 \times 10^{-6} \text{ s}^{-1}$ at 200 °C.

Table II. Fraction of Sliding GBs and Contribution of GBS to the Global Plastic Strain in the CG Material, Depending on Temperature, Strain, and Strain Rate

T (°C)	Strain Rate (s^{-1})	Strain Level (Pct)	Pct of Sliding GBs (Pct)	Contribution of GBS (Pct of Global Strain) (Pct)
100	1.5×10^{-5}	6	9	0.6
200	4.1×10^{-3}	12	44	0.8
200	1.8×10^{-3}	23	68	1.8
200	7.0×10^{-6}	5	55	3.8

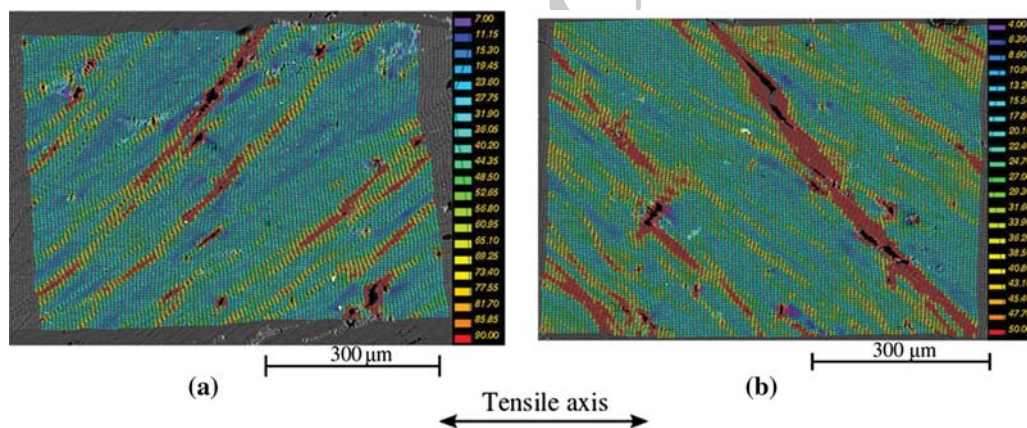


Fig. 11—Strain fields measured in F/UFG samples (a) at 100 °C, after 22.7 pct strain at $3 \times 10^{-6} \text{ s}^{-1}$ and (b) at 200 °C after 33.9 pct strain at $4.5 \times 10^{-3} \text{ s}^{-1}$.

365 identified model to investigate micro-scale cooperative
 366 phenomena (in terms of GBS and grains rotation) and
 367 their effects on the heterogeneity of the strain field.
 368 Crystal plasticity was thus not used, for the reasons
 369 evoked in the introduction: lack of representativeness of
 370 a single set of orientations that would call for repeated
 371 simulations, lack of data on non-octahedral slip systems,
 372 known to be active at the temperatures of interest.

373 In a first stage, to calibrate the model, adjust mesh
 374 parameters and investigate the effect of the number of
 375 simulated grains, equiaxed grains with a nearly uniform

size were considered. In a second stage, the model was
 applied to more realistic grains morphologies, inspired
 from the EBSD mapping shown on Figure 2.

A. Mesh and Boundary Conditions

For the first stage, various equiaxed microstructures
 were randomly generated using the classical Voronoi
 tessellation method. The mean grain size was controlled
 by the area of the simulation box, A_{box} and the number
 of grains, N :

$$d_{\text{grain}} = \sqrt{\frac{A_{\text{box}}}{N}} \quad [4]$$

387

388

389

390

391

392

393

394

395

396

397

398

399

400

401

402

403

404

405

406

407

408

409

It was adjusted to 680 nm, the mean grain size measured for the F/UFG material. A mesh with linear triangular elements for the grains and linear quadrilateral elements for the grain boundaries was adopted. After a convergence study, an element size equal to 0.01 times the simulation box edge was chosen along the GBs, and 0.05 times the simulation box edge for grain cores (Figure 14(a)).

Figure 14(a) presents the boundary conditions and loadings. The bottom left corner node was fixed and the vertical displacement of the bottom line was zero. A constant vertical displacement rate, \dot{U}_y , corresponding to a constant global strain rate, $\dot{\epsilon}$ was imposed at the top line, to simulate tensile tests, while a constant vertical displacement, corresponding to a fixed strain was applied to simulate stress relaxation. Due to the unavailability of periodic boundary conditions in the Disroc FE code, the left and right borders were free surfaces. One of the shortcomings of these boundary conditions was that the motions of GBs cutting a side surface are unconstrained and thus more pronounced than for GBs ending inside the model, while, conversely,

sliding of those cutting the upper or lower surface is more constrained. This bias however got smaller and smaller as the number of grains increased.

In a second stage, a more realistic microstructure with 262 grains (Figure 14(c)), inspired from the EBSD map shown on Figure 2(b), was designed, using the Voronoi tessellation method, but with the measured center of gravity of the grains used as “seeds” in the algorithm, instead of points randomly generated by a Poisson’s process. This makes it possible to take into account the heterogeneity of grains size and their elongated morphology. In addition, to reduce the above-mentioned artifact associated with unconstrained/over-constrained sliding of GBs cutting the sides of the model, a uniform buffer layer of material without sliding GBs, but with the same behavior as the grain cores was added all around, and the boundary conditions were applied on its external contour. The thickness of this external layer was equal to 1 grain diameter *i.e.*, for 262 grain model it was 6.2 pct of the edge of the central part.

B. Constitutive Equations for the Grains

The strain rate inside a grain was decomposed into elastic, plastic, and viscous components:

$$\dot{\epsilon}_g = \dot{\epsilon}_{el,g} + \dot{\epsilon}_{p,g} + \dot{\epsilon}_{v,g}. \quad [5]$$

The Young’s modulus $E(T)$ was temperature-dependent, while the Poisson’s ratio, ν , was assumed to remain constant. An isotropic strain hardening model was chosen. A Voce-type hardening function was adopted for the isotropic hardening variable, R :

$$R = R_0 + Q(1 - e^{-bp}), \quad [6]$$

where R_0 , Q and b are material constants, and p denotes the cumulated plastic strain. Von-Mises yield criterion is chosen. The yield function was thus:

$$\sqrt{3J_2(\sigma)} - R = 0. \quad [7]$$

The viscous strain inside the grains was calculated using an Arrhenius-type equation with power law in effective stress:

$$\dot{\epsilon}_{v,g} = a(\sigma - \sigma_c)^n, \quad [8]$$

where a and σ_c are temperature-dependent material parameters.

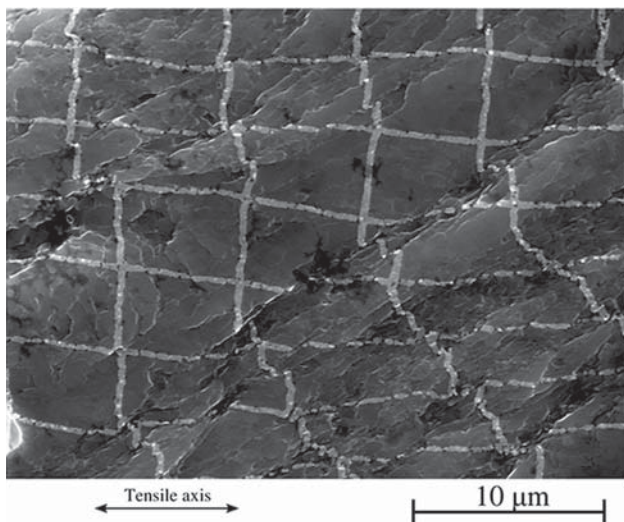


Fig. 12—Grain boundary sliding inside a shear band in a F/UFG sample strained by 49.8 pct at 200 °C at $1.4 \times 10^{-4} \text{ s}^{-1}$.

Table III. Contribution of GBS to the Global Plastic Strain in the F/UFG Material, Depending on Temperature, Strain, and Strain Rate

T (°C)	Strain Rate (s^{-1})	Strain Level (Pct)	Contribution of GBS (Pct of Global Strain) (Pct)
100	1.8×10^{-5}	12.9	9
100	3.0×10^{-6}	22.7	13
150	1.6×10^{-5}	27.5	22
200	4.5×10^{-3}	33.9	18
200	1.4×10^{-4}	49.8	29

456 1. *Constitutive equations for the grain boundaries*
 457 The displacement rate vector at a grain boundary had
 458 an elastic and a viscous component:
 459

$$\dot{U} = \dot{U}_{el} + \dot{U}_v. \quad [9]$$

461 The tangential and normal stresses were related to the
 462 elastic displacement by an elastic stiffness matrix, K :
 463
 464

$$\begin{pmatrix} \tau \\ \sigma \end{pmatrix} = \begin{pmatrix} K_t & K_{tn} \\ K_{nt} & K_n \end{pmatrix} \begin{pmatrix} U_t - U_{t,v} \\ U_n - U_{n,v} \end{pmatrix} \quad [10]$$

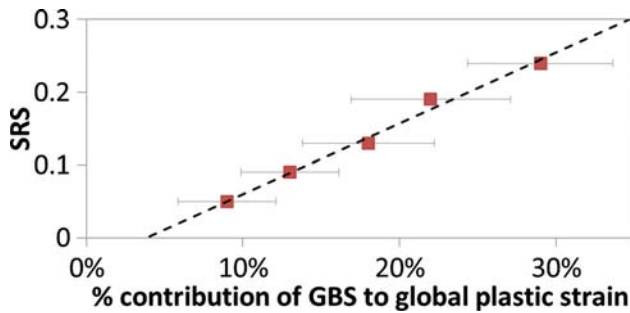


Fig. 13—Correlation between the strain rate sensitivity of the F/UFG alloy and the measured contribution of grain boundary sliding to its global deformation.

No tension-shear coupling was introduced, *i.e.*, both K_{nt} and K_{tn} were taken equal to zero. To limit the interpenetration of neighboring grains in case of normal compression, a hyperbolic expression was adopted for the normal stiffness, K_n .

$$K_n = \frac{K_0}{1 + \frac{U_n}{e}}, \quad [11]$$

where K_0 and e are constants. The closure displacement was thus limited by the initial (purely computational) “thickness”, e of the interface, taken as 1 pct of the simulation box size. Closure corresponds to negative values of U_n . The normal stiffness, K_n approaches infinity when the closure displacement, U_n tends to $-e$. The normal stress is proportional to the normal displacement for small openings (with a proportionality constant K_0) and saturates at $K_0 e$ for large positive openings (never reached in the present simulations). In order not to modify the global elastic behavior by elastic GBS, the GB elastic stiffness parameters, K_0 and K_t were not independent, but related to the Young’s and shear modulus, respectively.

For the viscous part, no normal creep was allowed, only viscous sliding was considered. A temperature-dependent threshold was introduced, *i.e.*, the sliding rate

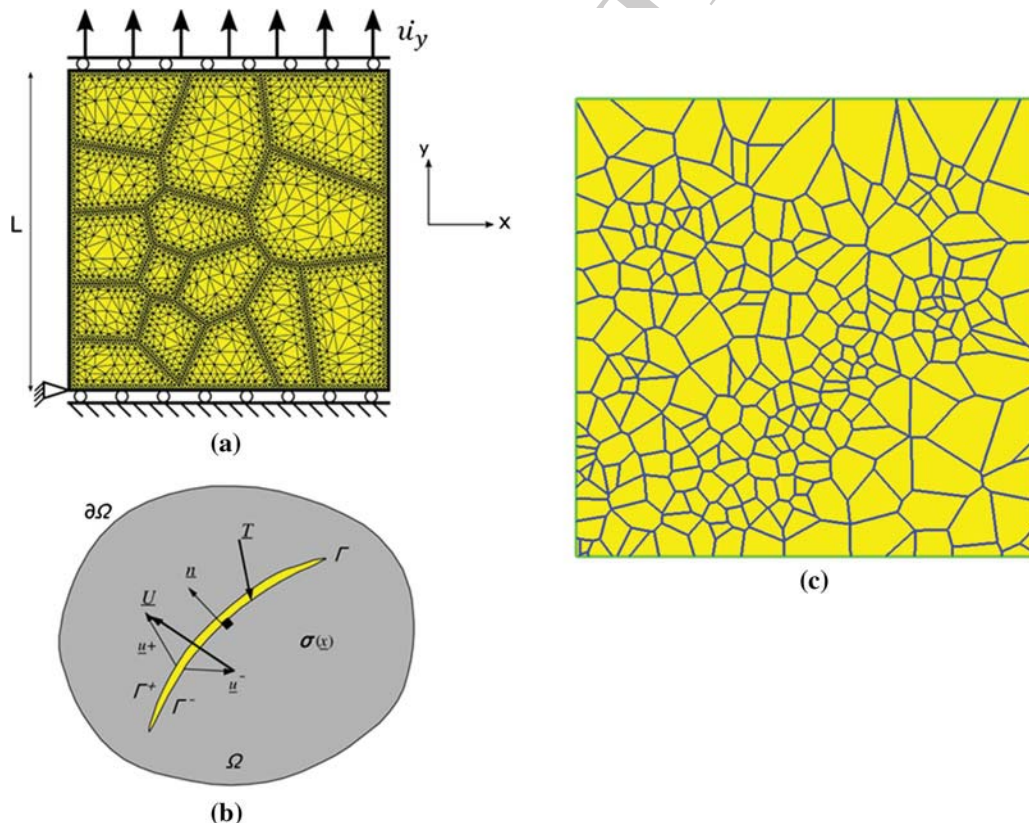


Fig. 14—(a) Example of mesh and boundary conditions used for the model calibration stage, (b) description of a sliding interface, and (c) more realistic microstructure inspired from the EBSD mapping shown on Fig. 2(b).

492 was supposed to be zero if the shear stress did not reach
 493 the threshold stress, τ_c , and was proportional to the net
 494 shear stress otherwise.

$$\dot{U}_{t,v} = b_t(\tau - \tau_c). \quad [12]$$

497 To take into account the thermally-activated nature
 498 of GB sliding, an Arrhenius-type expression inspired
 499 from the work of Raj and Ashby^[11] and Agarwal
 500 *et al.*^[19] was assumed for the proportionality constant:
 501
 502

$$b_t = \frac{b_0}{kT} e^{-\frac{Q_{GBS}}{kT}}, \quad [13]$$

504 where b_0 is a material parameter ($6.64 \times 10^{-28} \text{ m}^4 \text{ s}^{-1}$,
 505 according to Reference 18), Q_{GBS} is the activation
 506 energy for GBS ($1.4 \times 10^{-19} \text{ J}$, according to Reference
 507 18) and k is Boltzmann's constant.

508 The macroscopic viscoplastic strain E_{vp} sees the
 509 contributions from the matrix viscoplastic strain and
 510 from the viscous displacement jumps U_k across sliding
 511 interfaces of contour Γ_k and normal n_k (Figure 14(b)):
 512

$$E_{vp} = \frac{1}{V} \left[\int_V \varepsilon_{vp} \cdot dV + \sum_k \int_{\Gamma_k} \frac{1}{2} (U_{v,k} \otimes n_k + n_k \otimes U_{v,k}) ds \right]. \quad [14]$$

514 The contribution of GBS to the global viscoplastic
 515 strain can thus be computed as the second term of the
 516 right hand side of Eq. [14] divided by E_{vp} .
 517

518 2. Determination of the minimum number of simulated 519 grains for convergence

520 To determine the minimum number of grains required
 521 in the model so as to get rid of the scatter from one
 522 randomly-generated microstructure to the other—in
 523 terms of global stress–strain behavior, but also in terms
 524 of predicted contribution of GBS—, five different
 525 microstructures each with 15, 22 and 30 grains of
 526 similar mean grain size were randomly generated
 527 (Figure 15(a)). A tensile test up to 10 pct strain was
 528 simulated at $5 \times 10^{-3} \text{ s}^{-1}$ for each of these microstruc-
 529 tures, using the same parameters. The five simulated
 530 stress–strain curves for a given number of grains, as well
 531 as the evolutions of the contribution of GB sliding to the
 532 global strain are compared in Figures 15(b) and (c).

533 For the model with 15 grains, the difference between
 534 the maximum and the minimum predicted GBS contri-
 535 butions was as high as 25 pct. Model #1 and model #3
 536 showed the highest and the lowest contributions of
 537 GBS, respectively, which correlated well with their
 538 respective highest and lowest cumulated lengths of
 539 GBs projected on the maximum shear stress directions,
 540 and with the presence of well oriented GBs cutting free
 541 surfaces in model #1. Note that the highest contribution
 542 of GBS also corresponded to the softest macro-scale
 543 response, and *vice versa*. Macro-scale convergence was
 544 achieved for 22 grains, and the bias due to the free side
 545 surfaces was reduced as well. However, some scatter
 546 (approximately 5 pct difference) was still observed in the

contribution of GB sliding to the global strain. 547
 Microstructures with 30 grains had to be used to get 548
 reproducible stress–strain curves as well as reproducible 549
 predictions of GBS contribution. 550

551 3. Assumptions made and identification procedure

552 As a whole, 12 parameters, some of which tempera-
 553 ture-dependent, had to be identified. Out of those, only
 554 10 are actually independent, since K_0 and K_t were
 555 deduced from the global elastic moduli. The Young's
 556 modulus was identified from the tensile tests at each
 557 temperature. The hardening parameters R_0 , Q , and b
 558 were identified from the room temperature tensile tests.
 559 While b was assumed independent of the temperature,
 560 R_0 and Q were deduced from the yield stress, at each
 561 temperature. The three viscosity parameters of the
 562 grains, a , n and the threshold stress σ_c were identified
 563 from available tension and relaxation data. An initial
 564 guess for the GB sliding proportionality constant, b_t ,
 565 was obtained by extrapolating the equation provided by
 566 Agarwal *et al.*^[9] for A15083 for higher temperatures to
 567 the medium temperature range of interest.

568 C. Identified Model and Insight into Micro-scale 569 Phenomena

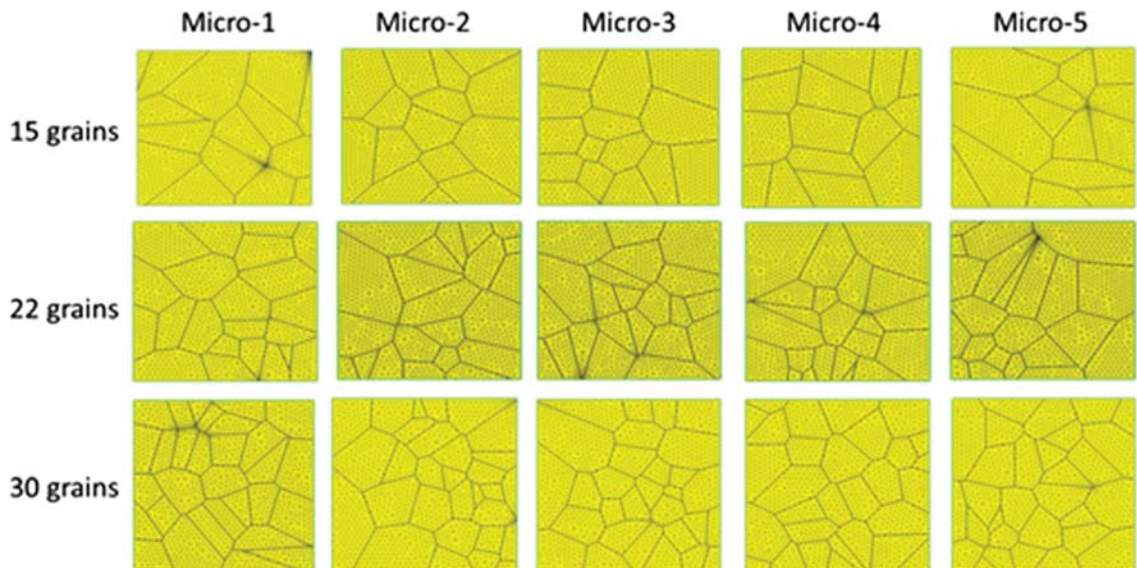
570 A comparison of experimental and simulated stress–
 571 strain or strain rate–stress curves at each temperature is
 572 shown on Figure 16, and the corresponding best-fit sets
 573 of parameters are gathered in Table IV.

574 The model captures the large change in tensile
 575 strength with strain rate for the F/UFG material. The
 576 simulated relaxation curve at 200 °C nicely reproduces
 577 the experimental one, while a less satisfactory agreement
 578 is obtained at 100 °C and 150 °C.

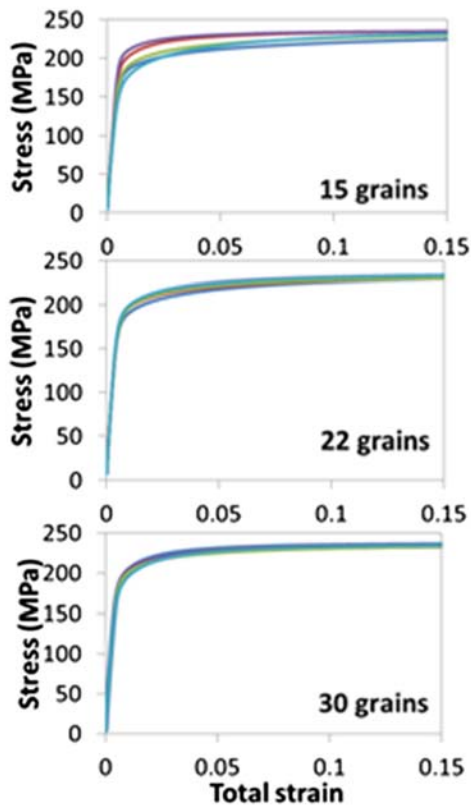
579 The contribution of grain boundary sliding during the
 580 simulated tensile tests is plotted *vs* the inelastic strain in
 581 Figure 17.

582 Because the threshold stress for GB sliding ($\approx 2 \times \tau_c$)
 583 was always lower than the threshold stresses for plastic
 584 and viscous flow inside the grains (R_0 and σ_c , respec-
 585 tively), 100 pct of the inelastic strain was initially
 586 accommodated by GB sliding. This fraction then
 587 decreased as inelastic deformation developed inside the
 588 grains, and tended towards a steady-state value, which
 589 was always much larger in the UFG material. Such
 590 evolutions bear some similitude with that of the ratio of
 591 plastic dissipation due to GBS to the total plastic
 592 dissipation computed for nano-crystalline copper by
 593 Warner *et al.*^[24] using atomistically-informed CPFÉ.
 594 This ratio also started at 100 pct and decreased towards
 595 a grain size-sensitive value. As expected, the contribu-
 596 tion of GBS was predicted to increase with decreasing
 597 strain rate at a given temperature (Figure 17(a)) and
 598 with increasing temperature, at a fixed rate
 599 (Figure 17(b)).

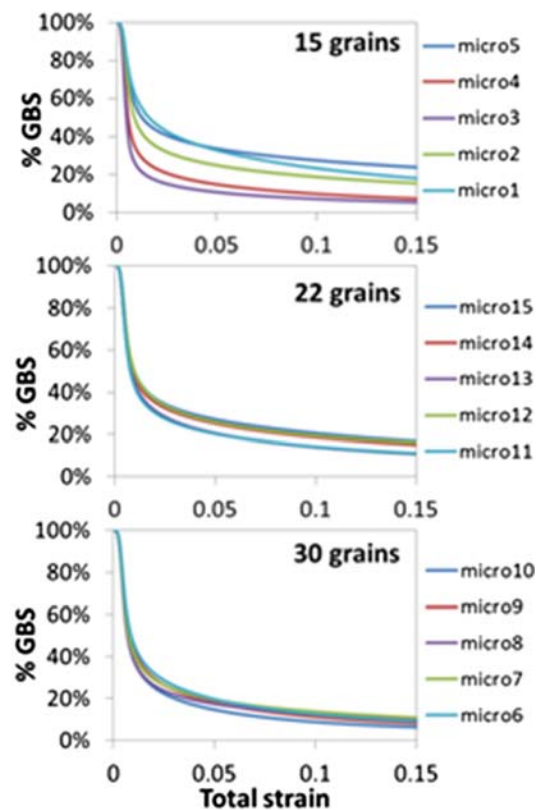
600 The SRS computed for the F/UFG material is plotted
 601 on Figure 18 *vs* the predicted contribution of GBS to the
 602 global inelastic strain, after 10 pct tensile strain, at
 603 various rates and temperatures. The experimental data
 604 are also plotted for comparison. The model captures the
 605 experimentally observed direct correlation.



(a)



(b)



(c)

Fig. 15—Convergence study in terms of number of grains: (a) meshes, (b) computed stress–strain curves, and (c) contribution of GBS to the global inelastic strain.

606 Figure 19 shows the viscous sliding along GBs at
 607 various stages of a tensile test at 200 °C and
 608 $2 \times 10^{-4} \text{ s}^{-1}$. Initially, GB sliding was triggered by
 609 the far field, and thus occurred along GBs oriented
 610 close to the maximum shear stress direction
 611 (± 45 deg), and often along less constrained,

surface-cutting GBs. Upon further straining, sliding 612
 was triggered along connected GBs, not as well 613
 aligned with the far-field shear stress, and were 614
 pushed by an already gliding GB. This led to 615
 cooperative GBS along “percolation paths” that 616
 sometimes crossed the gage width. This phenomenon 617

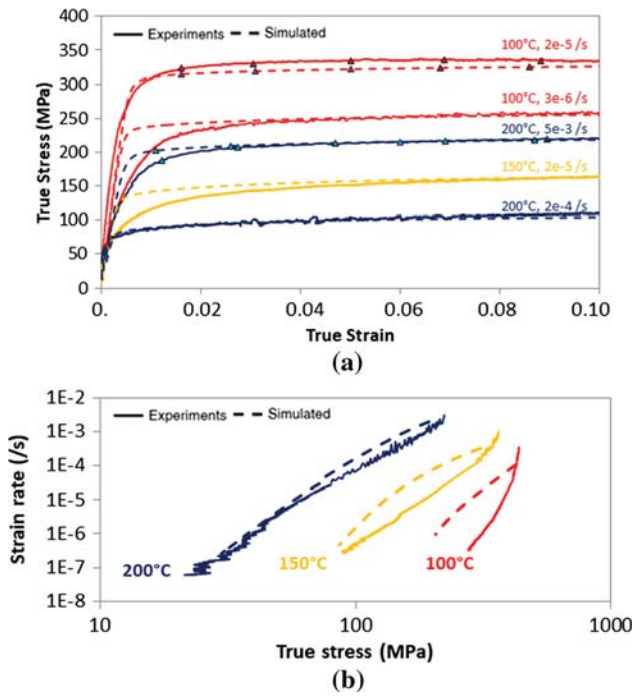


Fig. 16—Experimental and simulated curves for (a) tensile and (b) relaxation tests on F/UFG material at 100 °C, 150 °C, and 200 °C.

Table IV. Identified Set of Parameters

	100 °C	150 °C	200 °C
E (MPa)	62000	56900	51700
ν	0.3	0.3	0.3
R_0 (MPa)	325	292	225
Q (MPa)	125	75	50
b	45	45	45
a ($s^{-1} MPa^{-n}$)	1.5×10^{-18}	8.5×10^{-14}	2.5×10^{-12}
n	5.5	4	4
σ_c (MPa)	89	48	15
K_n ($MPa mm^{-1}$)	4.26×10^9	3.91×10^9	3.55×10^9
K_t ($MPa mm^{-1}$)	1.64×10^9	1.50×10^9	1.37×10^9
b_t ($mm s^{-1} MPa$)	2×10^{-10}	4.5×10^{-9}	5.0×10^{-8}
τ_c (MPa)	42	10	2

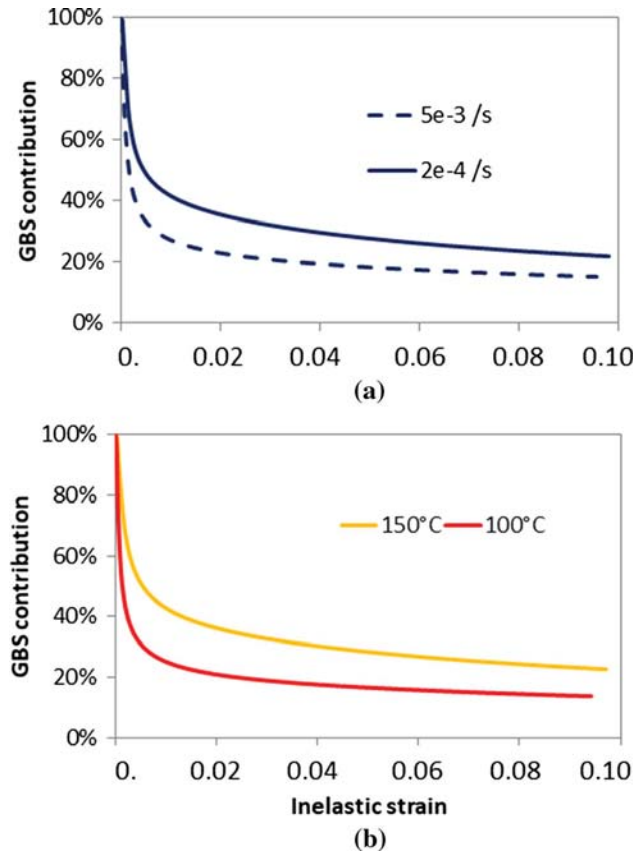


Fig. 17—Predicted effects of (a) strain and strain rate at 200 °C and (b) strain and temperature at $2 \times 10^{-5} s^{-1}$ on the contribution of GBS to the global inelastic strain in F/UFG material.

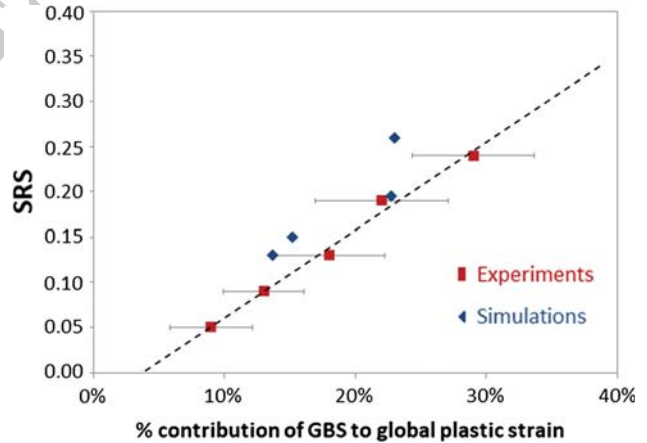


Fig. 18—Correlation between measured/computed SRS and measured/computed contribution of GBS to the global deformation.

618 might explain the intense shear bands crossing the
619 whole gage length observed in F/UFG material at
620 high temperature.

621 Figure 20 reports some simulation results for a tensile
622 test until 10 pct strain at $5 \times 10^{-3} s^{-1}$ and 200 °C on the
623 more realistic, heterogeneous microstructure shown on
624 Figure 14(c). Figure 20(a) shows the axial viscoplastic
625 strain field, Figure 20(b) shows the viscous sliding along
626 GBs, Figure 20(c) corresponds to the rotation field
627 (antisymmetric part of the displacement gradient), and
628 Figure 20(d) the average rotation in each grain. From
629 Figure 20(a), it appears that in some places (see the
630 enlarged areas), transgranular shear bands are induced
631 by sliding along a neighboring GB, which relaxes the
632 shear stress along the GB, so that this stress is
633 redistributed in the next grain, and triggers viscoplastic

634 flow. This intensified transgranular plastic flow might in
635 turn activate GBS along a GB located on the other side
636 of the grain. Percolation *through the grains* and not only
637 *along the GBs* might thus contribute to the development
638 of long shear bands.

639 It can also be concluded that GBS increases the
640 heterogeneity of the plastic strain field: a variation from
641 0.57 to 2.5 times the mean plastic strain is observed here,
642 in spite of similar constitutive equations in all the
643

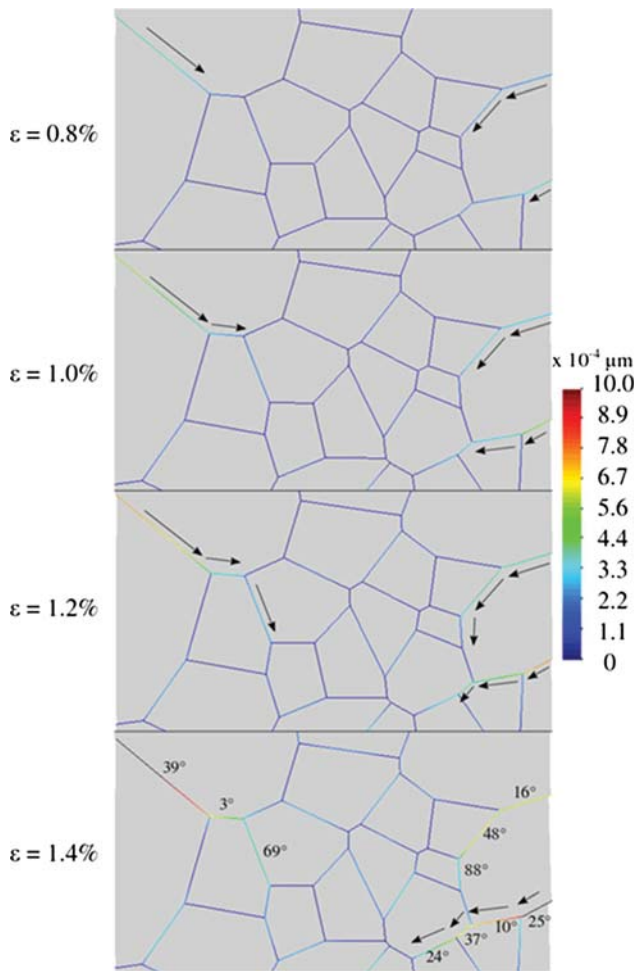


Fig. 19—Viscous sliding along GBs at various steps for a simulation run at $2 \times 10^{-4} \text{ s}^{-1}$ and $200 \text{ }^\circ\text{C}$ in the F/UFG material.

“grains”. Such a range is not so far from the range obtained by the statistical analysis of plastic strain fields measured by DIC in the F/UFG material, which was typically 0 to 3 times the mean value.^[21]

Time-dependent grains rotation has been shown, through *in situ* SEM or TEM straining and crystal orientation mappings, to contribute significantly to the viscoplastic deformation of UFG materials, even at room temperature^[30–32] and to be a collective process, occurring in small groups of neighboring grains.^[32] This feature is retrieved by the simulations, as illustrated by Figure 20(d), which shows clusters of grains rotated by up to $\pm 1.5 \text{ deg}$. Neighboring grains often exhibit rotations of opposite sign (as if they were contacting gears) so that the overall rotation vanishes. The formation of such grain clusters, often inclined by $\pm 45 \text{ deg}$ relative to the tensile axis, might also contribute to the development of shear bands. Figure 20(c) shows that grains do not rotate as a block. The rotation is generally more pronounced near their sliding GBs—where it can reach $\pm 5 \text{ deg}$, which should lead to an accumulation of geometrically-necessary dislocations—than in their core. Furthermore, GBS and grain rotation are clearly correlated phenomena: grains that do not exhibit GBS do not rotate significantly, and the largest rotations are associated with substantial GBS.

IV. CONCLUSIONS AND PERSPECTIVES

The boundary between the temperature-strain rate domains where the F/UFG Al 5083 alloy is stronger or softer than its CG counterpart was determined and is consistent with data from the literature (Figure 6).

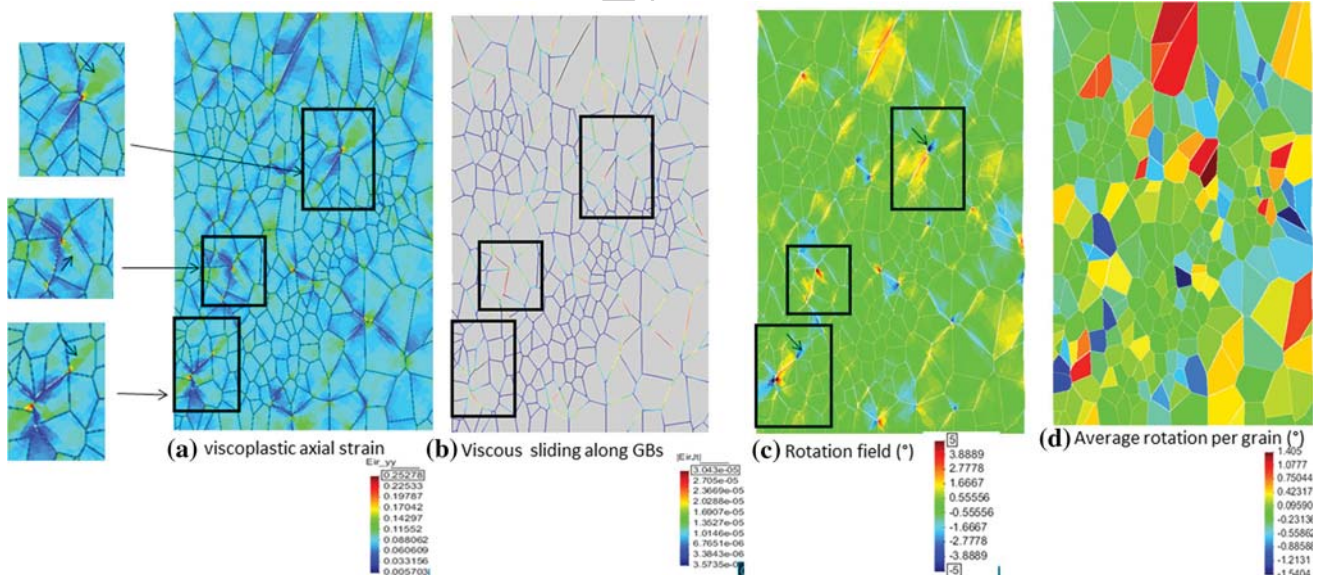


Fig. 20—Results from the simulation of a tensile test at $5 \times 10^{-3} \text{ s}^{-1}$ at $200 \text{ }^\circ\text{C}$ until 10 pct strain on the microstructure from Fig. 14(c).

674 The SRS of the F/UFG material, which is higher than
675 that of CG material, rises with the temperature and as the
676 strain rate decreases (Figure 5). It is controlled by grain
677 boundary sliding (Figure 13), and controls the ductility,
678 which is thus strongly rate-dependent (Figure 7).

679 Both CG and F/UFG materials exhibit more and
680 more GBS as the temperature rises and as the strain rate
681 decreases. However, in the former, this mechanism
682 accounts at most for 4 pct of the global strain below
683 200 °C, while in the latter, its contribution can reach
684 29 pct (Tables II and III).

685 A 2D phenomenological FE-model with viscoplastic
686 grains and viscous sliding GBs was developed and identi-
687 fied. It captured the macroscopic behavior of the F/UFG
688 material over a wide range of rates and temperatures.

689 The model also showed that GBS increases the
690 heterogeneity of the plastic strain field. It provided
691 some insight into the correlated and cooperative mech-
692 anisms of GBS and grain rotation that are probably
693 responsible for macro shear banding in the F/UFG
694 material. The simulations suggested that such coopera-
695 tive phenomena occur along percolation paths that can
696 be intergranular as well as transgranular.

697 Several further developments of the model can be
698 envisaged: (1) the uniform threshold stress for GB sliding
699 used here might rather be a random variable to capture
700 the differences in GBs ability to slide and (2) a grain size
701 dependence of the model parameters might be introduced.
702 The latter objective would however require a substantial
703 experimental database on several batches of material with
704 different mean grain size, for calibration.

705

706

ACKNOWLEDGMENTS

707 An ECAP facility of LEM3 laboratory in Metz was
708 used to produce the UFG material, under the supervi-
709 sion of Dr. J.J. Fundenberger, who is gratefully
710 acknowledged.


711

REFERENCES

1. Y. Huang and T.G. Langdon: *Mater. Today*, 2013, vol. 16, pp. 85–93.
2. I. Sabirov, M.R. Barnett, Y. Estrin, and P.D. Hodgson: *Scripta Mater.*, 2009, vol. 61, pp. 181–84.
3. K.V. Ivanov and E.V. Naydenkin: *IOP Conf. Ser. Mater. Sci. Eng.*, 2014, vol. 63, pp. 1–10.

4. R.C. Gifkins, A. Gittins, R.L. Bell, and T.G. Langdon: *J. Mater. Sci.*, 1968, vol. 3, pp. 306–13.
5. A. Arieli and A.K. Mukherjee: *Mater. Sci. Eng.*, 1980, vol. 45, pp. 61–70.
6. Y.G. Ko, D.H. Shin, K.T. Park, and C.S. Lee: *Mater. Sci. Eng. A*, 2007, vols. 448–451, pp. 756–60.
7. K.-T. Park, L.Y. Hwang, S.-Y. Chang, and D.H. Shin: *Metall. Mater. Trans. A*, 2002, vol. 33A, pp. 2859–67.
8. K.T. Park, H.J. Lee, C.S. Lee, B.D. Ahn, H.S. Cho, and D.H. Shin: *Mater. Trans.*, 2004, vol. 45, pp. 958–63.
9. S.Y. Chang, L. Jung Guk, K.T. Park, S. Dong Hyuk, J.G. Lee, K.T. Park, and D.H. Shin: *Mater. Trans.*, 2001, vol. 42, pp. 1074–80.
10. R. Kapoor and J.K. Chakravartty: *Acta Mater.*, 2007, vol. 55, pp. 5408–18.
11. R. Raj and M.F. Ashby: *Metall. Trans.*, 1971, vol. 2, pp. 1113–27.
12. M.F. Ashby and R.A. Verrall: *Acta Metall.*, 1973, vol. 21, pp. 149–63.
13. F. Crossman and M.F. Ashby: *Acta Metall.*, 1975, vol. 23, pp. 425–40.
14. V. Tvergaard: *J. Mech. Phys. Solids*, 1985, vol. 33, pp. 447–69.
15. V. Tvergaard: *Rev. Phys. Appl.*, 1988, vol. 23, pp. 595–604.
16. K.J. Hsia, D.M. Parks, and A.S. Argon: *Mech. Mater.*, 1991, vol. 11, pp. 43–62.
17. P. Onck and E. Van der Giessen: *Int. J. Solids Struct.*, 1997, vol. 34, pp. 703–26.
18. A.F. Bower and E. Wininger: *J. Mech. Phys. Solids*, 2004, vol. 52, pp. 1289–1317.
19. S. Agarwal, C.L. Briant, P.E. Krajewski, A.F. Bower, and E.M. Taleff: *J. Mater. Eng. Perform.*, 2007, vol. 16, pp. 170–78.
20. N. Du, A.F. Bower, P.E. Krajewski, and E.M. Taleff: *Mater. Sci. Eng. A*, 2008, vol. 494, pp. 86–91.
21. A. Goyal, Mechanical behaviour of ultra-fine grain Al 5083 alloy: Analysis and modelling of the role of grain boundaries to overall plastic deformation., Ph.D. Thesis, Ecole Polytechnique, Palaiseau, France, 2018.
22. Y. Qi and P.E. Krajewski: *Acta Mater.*, 2007, vol. 55, pp. 1555–63.
23. N. Du, Y. Qi, P.E. Krajewski, and A.F. Bower: *Metall. Mater. Trans. A*, 2011, vol. 42A, pp. 651–59.
24. D.H. Warner, F. Sansoz, and J.F. Molinari: *Int. J. Plast.*, 2006, vol. 22, pp. 754–74.
25. L. Allais, M. Bornert, T. Bretheau, and D. Caldemaison: *Acta Metall. Mater.*, 1994, vol. 42, pp. 3865–80.
26. D. Lee: *Metall. Trans.*, 1971, vol. 2, pp. 1245–48.
27. R. Kapoor, C. Gupta, G. Sharma, and J.K. Chakravartty: *Scripta Mater.*, 2005, vol. 53, pp. 1389–93.
28. R.L. Bell, C. Graeme-Barber, and T.G. Langdon: *Trans. Metall. Soc. AIME*, 1967, vol. 239, pp. 1821–23.
29. Fracsima, Disroc, a Finite Element Code for modelling Thermo-Hydro-Mechanical processes in fractures porous media. 2016. <http://www.fracsima.com/DISROC/Disroc.html>.
30. Yu. Ivanisenko, N.A. Enikeev, K. Yang, A. Smoliakov, V.P. Soloviev, and H. Fecht: *Mater. Sci. Eng. A*, 2016, vol. 668, pp. 255–62.
31. E. Izadi, A. Darbal, R. Sarkar, and J. Rajagopalan: *Mater. Des.*, 2017, vol. 113, pp. 186–94.
32. F Mompou and M Legros: *Scripta Mater.*, 2015, vol. 99, pp. 5–8.

Publisher's Note Springer Nature remains neutral with regard to jurisdictional claims in published maps and institutional affiliations.

	Journal : MMTA	Dispatch : 3-12-2019	Pages : 14
	PIPS No. : 5583	<input type="checkbox"/> LE	<input type="checkbox"/> TYPESET
	MS Code :	<input type="checkbox"/> CP	<input type="checkbox"/> DISK